The detection of energetic electrons with the Cassini Langmuir probe at Saturn

P. Garnier,[1,2] J.-E. Wahlund,[3] M. K. G. Holmberg,[3] M. Morooka,[3] S. Grimald,[1,2] A. Eriksson,[3] P. Schippers,[4] D. A. Gurnett,[4] S. M. Krimigis,[5,6] N. Krupp,[7] A. Coates,[8] F. Crary,[9] and G. Gustafsson[3]

Received 25 October 2011; revised 29 August 2012; accepted 30 August 2012; published 3 October 2012.

[1] The Cassini Langmuir probe, part of the Radio and Plasma Wave Science (RPWS) instrument, has provided a wealth of information about the cold and dense plasma in the Saturnian system. The analysis of the ion side current (current for negative potentials) measured by the probe from 2005 to 2008 reveals also a strong sensitivity to energetic electrons (250–450 eV). These electrons impact the surface of the probe, and generate a detectable current of secondary electrons. A broad secondary electrons current region is inferred from the observations in the dipole L Shell range of ∼6–10, with a peak full width at half maximum (FWHM) at L = 6.4–9.4 (near the Dione and Rhea magnetic dipole L Shell values). This magnetospheric flux tube region, which displays a large day/night asymmetry, is related to the similar structure in the energetic electron fluxes as the one measured by the onboard Electron Spectrometer (ELS) of the Cassini Plasma Spectrometer (CAPS). It corresponds spatially to both the outer electron radiation belt observed by the Magnetosphere Imaging Instrument (MIMI) at high energies and to the low-energy peak which has been observed since the Voyager era. Finally, a case study suggests that the mapping of the current measured by the Langmuir probe for negative potentials can allow to identify the plasmapause-like boundary recently identified at Saturn, and thus potentially identify the separation between the closed and open magnetic field lines regions.

Citation: Garnier, P., et al. (2012), The detection of energetic electrons with the Cassini Langmuir probe at Saturn, *J. Geophys. Res.*, *117*, A10202, doi:10.1029/2011JA017298.

1. Introduction

[2] The Langmuir probe onboard the Cassini spacecraft—referred to as LP in the paper—is one of the sensors of the Radio and Plasma Waves experiment [*Gurnett et al.*, 2004] and is dedicated to the measurement of parameters of cold (below temperatures of ∼5 eV) and dense plasmas (above several particles per cm^3). The LP provides primarily a wealth of information about Titan's ionosphere: its overall structure [*Wahlund et al.*, 2005a; *Garnier et al.*, 2009], its ionization sources [*Ågren et al.*, 2007], electrodynamics [*Rosenqvist et al.*, 2009; *Ågren et al.*, 2011], as well as escape processes [*Modolo et al.*, 2007; *Edberg et al.*, 2010, 2011]. In addition, the LP allowed the investigation of other cold plasma environments such as the Saturnian plasma disk [*Wahlund et al.*, 2005b; *Morooka et al.*, 2009; *Jacobsen et al.*, 2009; *Gustafsson and Wahlund*, 2010] and of dusty regions such as the Enceladus plume or the rings environment [*Wahlund et al.*, 2009; *Morooka et al.*, 2011].

[3] Beyond cold plasma observations, we will demonstrate in this paper that the LP is also very sensitive to more energetic electrons (the adjective "energetic" will refer to energies around ∼250–450 eV in this paper). After a brief description of the various currents measured by the LP (section 2.1), we show the presence of a secondary electrons current region (the word "current" will refer to the currents measured by the probe from the collection of particles at its surface, and not to a real plasma current) in-between the magnetic L-shells 6–10 from the analysis of LP data during several years (section 2.2). We then describe how we extract this current of secondary electrons from the probe measurements (section 3). The comparison between this extracted current and the Cassini CAPS (Cassini Plasma Spectrometer) and MIMI (Magnetosphere Imaging Instrument) particles data leads to the identification of the source

[1]Université de Toulouse, UPS-OMP, IRAP, Toulouse, France.
[2]CNRS, IRAP, Toulouse, France.
[3]Swedish Institute of Space Physics, Uppsala, Sweden.
[4]Department of Physics and Astronomy, University of Iowa, Iowa City, Iowa, USA.
[5]Johns Hopkins University Applied Physics Laboratory, Laurel, Maryland, USA.
[6]Office for Space Research and Technology of Athens, Athens, Greece.
[7]Max-Planck-Institut fur Sonnensystemforschung, Katlenburg-Lindau, Germany.
[8]Mullard Space Science Laboratory, University College London, London, UK.
[9]Southwest Research Institute, San Antonio, Texas, USA.

Corresponding author: P. Garnier, CNRS, IRAP, 9, avenue du Colonel Roche, BP 44346, FR-31028 Toulouse CEDEX 4, France. (philippe.garnier@irap.omp.eu)

©2012. American Geophysical Union. All Rights Reserved.
0148-0227/12/2011JA017298

particles creating the region of enhanced current observed (section 4.1), and to the explanation of the morphology of this region (section 4.2). A case study suggests that mapping the current of the LP for negative potentials can allow us to identify the plasmapause-like boundary recently identified by *Gurnett et al.* [2010] at Saturn (section 4.2). Finally, a summary of our results and perspectives end this article (section 5).

2. Langmuir Probe Observations

2.1. Description of the Currents Measured by the Langmuir Probe

[4] The LP consists of a Titanium Nitride (TiN) coated conductive Titanium sphere (radius of 2.5 cm) mounted on a boom (length of 1.5 m). The bias voltage of the probe (U_B, actively applied to the LP with respect to the spacecraft) is varied every 10 minutes between −32 V and +32 V (or −4 V and +4 V every 24 s during certain Titan flybys), allowing the detection of electrons or ions depending on the sign of the potential U relative to the plasma ($U = U_B + V_{float}$ with V_{float} being the floating potential of the probe). The LP can be used to determine plasma parameters such as the electron density and temperature, the ion bulk flow speed and total energy (ram and thermal energy), as well as the spacecraft potential.

[5] The derivation of these parameters is based on the fitting of the current-voltage (I-V) curve [e.g., *Fahleson et al.*, 1974] using the Orbital Motion Limited (OML) theory [e.g., *Mott-Smith and Langmuir*, 1926]. This paper deals with the thin magnetospheric plasma where the Debye length is much larger than the probe radius, which justifies the use of OML theory: e.g. the Debye length is larger than 2.5 m for a typical equatorial plasma near $L = 6$ with a density of 30 cm^{-3} and a temperature of 4 eV [*Persoon et al.*, 2009]. It should be made clear that the currents are collected with no information about their precise direction. This has no impact for our study, since the investigation of anisotropies of the plasma collected is beyond the scope of the paper.

[6] The current (I_-) measured for negative potentials (U), later called ion side current, is given by:

$$I_- = I_{ions} + I_{el} + I^* + I_{dust} + I_{ph} + I^d_{sec} + I^*_{sec} \quad (1)$$

The first four currents are due to the incoming plasma, whereas the three last currents are related to the probe itself. I_{ions} and I_{el} are the (thermal and ram) currents due to the ambient cold ions and electrons, I_{dust} is the direct charged dust current to the probe, I^* the current due to direct impact of energetic electrons and ions, I_{ph} the photoelectron current (due to photoionization of the probe surface), I^d_{sec} the current of secondary electrons induced by the impact of dust, and I_{sec}^* the current of secondary electrons induced by the impact of energetic particles. In previous studies concerned with the analysis of Langmuir probe data in the magnetosphere, only the ram/thermal ion and photoelectron currents were usually considered for negative probe potentials: cold thermal electrons are repelled by the probe, dust particles are confined at the equator and the contribution by energetic particles was not taken into account.

[7] The current is linearly dependent on the bias potential for strong negative U_B values, so that I_- may also be parameterized by the following equation during the data analysis process [*Holmberg*, 2010, also submitted manuscript, 2012]:

$$I_- = m - bU_B \quad (2)$$

where m and b are respectively the level and slope of the fitted current-voltage (I-V) curve on the ion side; only strong negative bias potentials—"$U_B < -5$ V"—are included in the fitting process to remove the contribution of incoming cold electrons (I_{el}) which are not all repelled by small negative potentials: e.g. cold electrons with a temperature of 1 eV and a density of 10 cm^{-3} generate a small current of 10 pA for $U = -5$ V, 20 times smaller than the corresponding ion current.

[8] The photoelectron current was estimated from a detailed analysis [*Holmberg*, 2010, also submitted manuscript, 2012] of the currents measured in the outer magnetosphere and where the electron density is small ($n_e < 0.05$ cm^{-3}), i.e. in regions where only the photoelectron current can contribute. It was corrected for the attitude of the spacecraft and the location of the probe, and a proxy was finally derived for I_{ph} as a function of the F10.7 index ($W/m^2/Hz$), itself a commonly used proxy for solar extreme UV radiations [*Tapping*, 1987; *Dudok de Wit et al.*, 2009].

[9] The m current—DC level of the current measured on the ion side—has a random noise level of 0.1 nA (measured in laboratory; J. Wahlund, private communication, 2012). The derivation of the photoelectron current induces both a random noise level of 0.05 nA and a possible systematic error below 0.1 nA [*Holmberg*, 2010, also submitted manuscript, 2012, private communication, 2012]. The systematic error may be induced by several issues which are today not taken into account, such as a partial shadowing of the probe surface from a boom or an antenna, partial ring eclipses, etc. The noise levels will be considered in the paper, whereas the systematic error will not affect our results which are based on temporal correlations or comparisons between radial (L Shell) profiles.

2.2. A Secondary Electrons Current Region Observed

[10] Figure 1 gives a map of the ion current level ($m_{ion} = |m - I_{ph}| = -(m - I_{ph})$; see section 3.1 for the derivation of I_{ph}) for two different coordinate systems. The LP sweep data from February 1*st* 2005 to July 30*rd* 2008 were included (more than 250 000 measurements), and averaged inside each map cell of both panels (with size bins of 0.5 R_S—$R_S = 60268$ km—and bins of ∼40 minutes for Saturnian local time). Each cell contains more than hundred measurements on average, up to more than thousand in the inner magnetosphere near the equatorial plane. However, the inhomogeneous sampling of Saturn's environment by the Cassini spacecraft, with more events in the equatorial plane or near ±45° in latitude, probably induces a bias in the Figure 1, with increased uncertainties for the cells less sampled.

[11] A broad region was thus observed with a maximum in the L Shell range of ∼6–10 (see section 4.2 for a radial profile) near Dione and Rhea, and a clear organization along the L Shell values up to high latitudes (the red and blue lines represent dipolar magnetic field lines). Significant currents

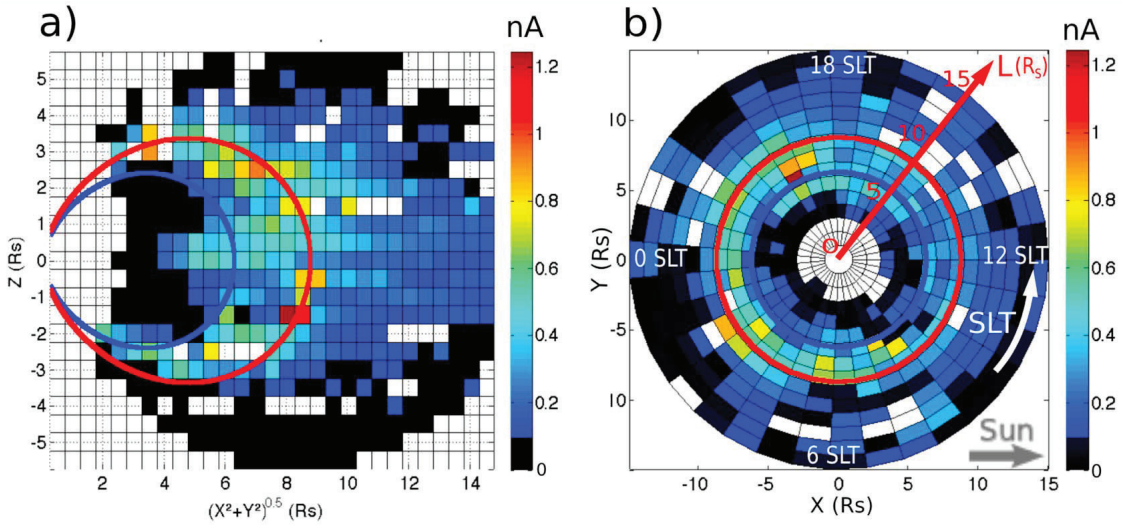

Figure 1. Maps in two coordinate systems of the current level (color-coded, white when there are no data, black for current values below the noise level of 0.11 nA) measured on the ion side by the LP and without the photoelectron contribution ($m_{ion} = |m - I_{ph}|$), from February 1st 2005 to July 30rd 2008. The thick blue and red lines show respectively the L Shell values [*McIlwain*, 1961] of Dione and Rhea. (a) (X, Y, Z) is the Saturn centered equatorial coordinate system (KSE or Kronocentric Saturn Equatorial), with Z pointing northward along Saturn's spin axis, X in the Saturn equatorial plane and positive toward the Sun, and $\vec{Y} = \vec{Z} \times \vec{X}$. (b) *SLT* gives the Saturnian local time.

above the background were also measured in the outer magnetosphere (up to at least $L = 14$ in the figure).

[12] Figure 1b also shows a clear local time asymmetry with larger values on the nightside (see also section 4.2). Strong currents were also observed near Saturn in the equatorial plane (see the cells inside the Dione L-shell and for $|Z| < 1\ R_S$), due to cold ions or electrons, but this aspect is out the scope of the paper.

[13] Which process may induce such large currents at any latitude among the sources listed in equation (1)? Only the effect of energetic particles ($I_{ener} = I^* + I_{sec}^*$) can actually account for the enhanced current region observed, since: the photoelectron current was already removed (and does not depend on the magnetospheric region but on solar activity and the spacecraft attitude), the cold ion thermal or ram current is much stronger near the equator where the dominating water group ions are centrifugally confined [*Sittler et al.*, 2008], the incoming cold electrons are negligible and the dust (as well as its induced current) is absent at high latitudes.

[14] To further understand these observations, it is required to isolate the energetic current I_{ener} and to analyze its source particles, in order to better understand the LP behavior regarding the current induced by energetic particle impact.

3. Derivation of the Energetic Current

[15] We will here analyze the LP observations in more details: we develop the method allowing to extract the current I_{ener} from the total ion side current I_- (3.1), and then two case studies are considered (3.2).

3.1. Description of the Method

[16] Starting from equation (1) and the knowledge of I_-, we can reduce the difficulty for isolating the energetic current I_{ener} if we focus on regions off the equatorial plane (e.g. $|Z| > 1\ R_S$), which removes the contributions by dust and reduces significantly the influence of cold ion currents to the probe. One needs only to estimate the contributions by cold ions (I_{ions}) and photoelectrons (I_{ph}).

[17] The cold ion current I_{ions} (containing both thermal and ram contributions) varies linearly with respect to the potential for negative U ($U = U_B + V_{float}$) values:

$$I_{ions} = I_{i_0} - bU \tag{3}$$

with I_{i_0} the "random ion current" given by the various contributions of each ith ion species [*Fahleson et al.*, 1974]:

$$I_{i_0} = -\sum_i A_{LP} n_i q_i \sqrt{\frac{v_i^2}{16} + \frac{k_B T_i}{2\pi m_i}} \tag{4}$$

with A_{LP} the surface of the probe, k_B the Boltzmann constant and n_i, T_i, q_i, v_i, m_i the density, temperature, charge state, drift speed (in the frame of the LP), mass of the ith ion species which are parameters not provided for each species by the LP (it can provide global—density weighted—values but cannot separate the contribution of each ion species).

[18] The combination of equations (1), (2) and (3) leads to the estimated energetic current outside the ring plane:

$$I_{ener} = m + bV_{float} - I_{i_0} - I_{ph} \tag{5}$$

[19] As a consequence, understanding the exact signature of energetic particles through the extraction of the associated current I_{sec}^* needs, at first, not only the analysis of the LP data, but also the analysis of ion data with the CAPS experiment [*Young et al.*, 2004] to estimate I_{i_0} (see section 3.2 for more details). We will now use the method to extract I_{ener} during

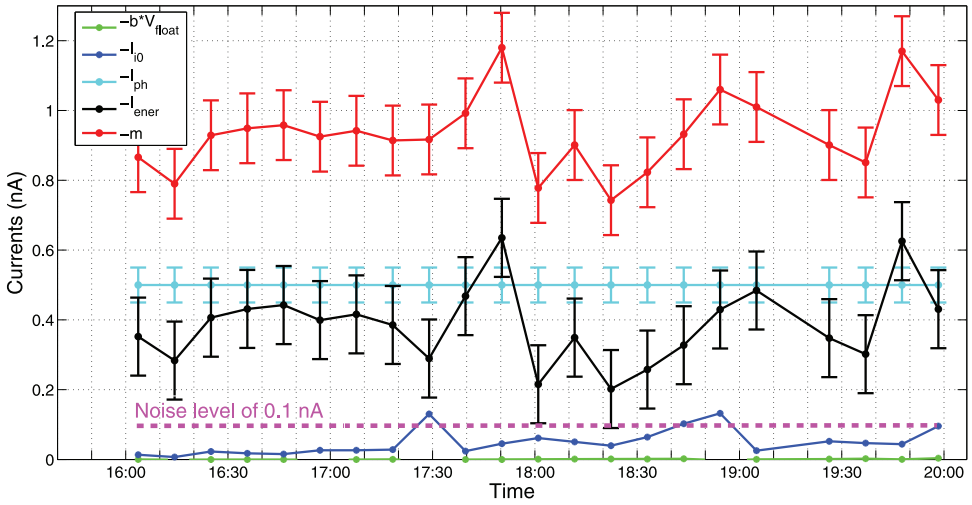

Figure 2. Currents (A) contributing to the total current I_{-} (measured for negative potentials) during the inbound leg of SOI (June 30th 2004) as a function of time. Negative values of currents are plotted since collected ion currents or emitted secondary electron currents are negative. The random noise level of 0.1 nA is overplotted in pink, and error bars are given for I_{ener} (±0.11 nA), m (±0.1 nA) and I_{ph} (±0.05 nA).

two specific time periods where the Cassini spacecraft crossed the enhanced current region—identified in section 2.2—off the equator.

3.2. Case Studies

[20] Two time periods were used: the SOI (Saturn Orbit Insertion) and a high inclination orbit in 2008.

[21] During the inbound part of SOI (June 30th 2004), from 16:00 to 20:00 UT, the Cassini spacecraft was located near the peak shown in Figure 1 and outside the dust region, in the L Shell range of 7–10 and at Z values below −1.2 R_S. The random ion current I_{i_0} was calculated using the SOI ion moments (i.e. n_i, T_i, v_i) derived from the analysis of the CAPS IMS data [*Sittler et al.*, 2006]. The two ion species identified by CAPS were included in I_{i_0}: water group ions (m_W = 17 amu) and protons (m_H = 1 amu). The velocity vector of the ion i with respect to the probe ($\overrightarrow{v_i} = \overrightarrow{V_{ion_i}} - \overrightarrow{V_{Cassini}}$) was calculated for each ion species and at each time interval, V_{ion_i} including the corotation and radial velocities profiles published by *Sittler et al.* [2006]. We considered only one radial velocity profile (average value over both species profiles published), the vertical velocity was neglected and no temperature anisotropy was taken into account by the authors. We will see later that these simplifications have no influence on our results, since the current I_{i_0} is small in our case studies.

[22] Figure 2 shows all currents (except dust currents) contributing to the ion side current I_{-} during SOI, with in particular the estimated energetic current $I_{ener} = I^* + I_{sec}^*$. We note that $b.\ V_{float}$ is almost zero, so that the total current I_{-} is directly given by the current level m (see equation (2)). The random ion current I_{i_0} driven by cold ions contributes up to 15% maximum only (at 17:30), about the same order of the LP current noise level (∼0.1 nA). As a result, the m current is itself dominated by I_{ph} and I_{ener} (since $m = I_{ener} - bV_{float} + I_{i_0} + I_{ph}$ from equation (5)). This confirms that energetic particles (I_{ener}) create the enhanced current region, since the second significant current (photoelectron current) is roughly stable at the scale of several hours, and thus cannot exhibit the temporal variability seen in the total current.

[23] A second period was analyzed, during a high inclination orbit on May 17th and 18th 2008, respectively at 19:30–20:10 and 1:40–2:10 during the inbound and outbound legs of the orbit. The analysis of all currents contributing to I_{-} revealed a similar situation to SOI (the results are not shown), with an energetic current of the same order as the photoelectron current, and a negligible influence by $b.V_{float}$. The spacecraft was located inside the secondary electron current region and well off the equator at $|Z|$ values above ∼2.75 and 2.45 R_S respectively, and in the L Shell ranges of 7.4–9.9 and 7–9.6.

[24] The contribution by cold ions (I_{ions}) was not removed during this second period. However, given the large $|Z|$ values —the dominating water group ions are mostly confined near the equator [*Thomsen et al.*, 2010]—and the small contribution during SOI for such particles, we could reasonably assume a small contribution of I_{ions}. We checked this assumption with a rough calculation of the cold ion current I_{i_0} based on density and temperature profiles published by *Thomsen et al.* [2010] and *Persoon et al.* [2009]: $I_{i_0} \sim 0.11$ and 0.18 nA for $|Z| = 2\ R_S$ and at respectively $L = 6$ and 10 R_S, thus leading to a value similar to the SOI current value, small enough to be neglected as a first step in our study. The broad data set of ion measurements published by *Thomsen et al.* [2010] will be used in a future study which will more focus on the quantitative side.

4. The Influence of Energetic Electrons

[25] The previous sections allowed to identify the current I_{ener} as the reason for the enhanced current region observed in Figure 1, and to extract it from the measurements. We will here perform a correlation analysis to identify the particles which induce this energetic current (section 4.1), and then investigate why the resulting signature has the observed shape (section 4.2).

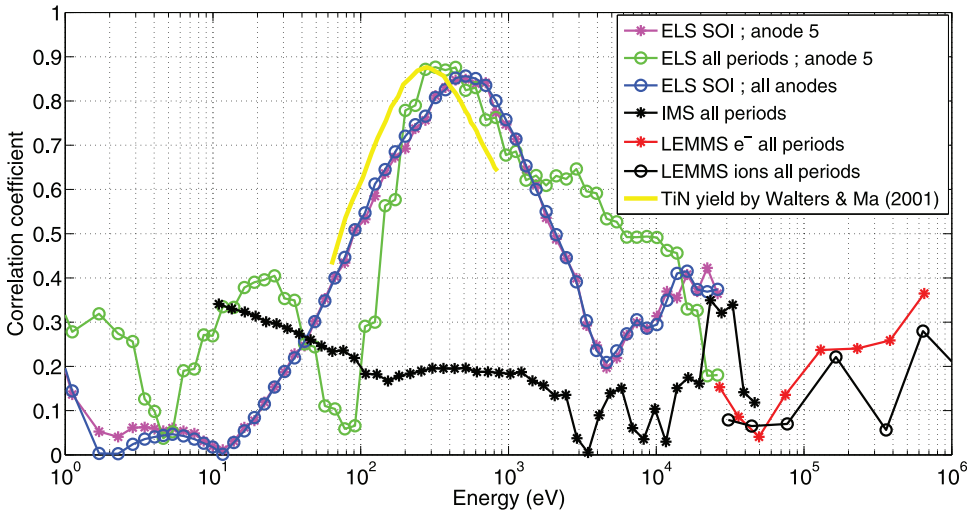

Figure 3. Pearson's correlation coefficient between the temporal evolutions of the current induced by energetic particles ($I_{ener} = I_{sec}^* + I^*$) and the particles fluxes—electrons (e-) and ions—as a function of the particles energy; "all periods" refers to both the SOI and the high inclination orbit periods. The secondary electron emission yield curve by *Walters and Ma* [2001] is plotted in yellow and normalized so that the maximum yield is placed at the same ordinate value as the maximum value of the green curve.

4.1. Identification of the Source Particles

[26] The derivation of the energetic current I_{ener}, which creates the secondary electron current region, allowed us to identify its source particles by comparison with the particles data from the MIMI LEMMS (Low Energy Magnetospheric Measurement System; described by *Krimigis et al.* [2004]) and CAPS ELS/IMS instruments (Electron Spectrometer/Ion Mass Spectrometer; described by *Young et al.* [2004]). Both contributions to the energetic current (I_{sec}^*, I^*) are proportional to the energetic particles fluxes. The principle of the analysis was thus to calculate the Pearson's r correlation coefficient [*Press et al.*, 2007] between the temporal evolutions of I_{ener} and of the particles fluxes, as a function of the energy of the incoming particles. The best correlation then indicated the source particles for the energetic current contribution to the LP.

[27] We analyzed the differential number fluxes (keV.cm^2.sr. s)$^{-1}$ for ions—with protons being the most significant energetic ion population up to high latitudes—and electrons during the time periods discussed in the previous section. We used the CAPS ELS electron data from anode 5 (the least affected by spacecraft structures) with all 63 energy channels from 0.53 eV/q (lower value of bin number 63) up to 28.3 keV/q (upper value of bin number 1). The low energy ion fluxes were provided by the CAPS IMS energy channels from 0.01 to 50.3 keV (from the anodes oriented toward the corotation direction; R. Wilson, private communication, 2011).

[28] The CAPS ELS data were corrected for the rare unphysical negative values introduced by the software used, but neither for noise nor for other artifacts such as the obscuration of parts of the spacecraft bus, or the focusing of electrons in the non-uniform spacecraft potential. Since our data correspond to regions outside the radiations belts, the noise which might affect our analysis mostly comes from the radiation sources of the spacecraft (i.e. the radioisotope thermoelectric generators). This background noise level affects all energy channels and its value was estimated by *Arridge et al.* [2009] below the one-count level of ~42 *counts/s*, between 20 and 30 *counts/s* for the anode 5 [see *Arridge et al.*, 2009, Figure A2], depending on the orientation of the spacecraft, the actuator position and the averaging of the data. During the time periods considered, the mean signal-to-noise ratio—for a noise level of 30 *counts/s*—decreased from 240 to 3.1 with energy (from bin number 63 to bin number 1), with mean values near 32 or 33 for 250–450 eV electrons (and minimum/maximum values of 9/80 among the time steps). Furthermore, the data were averaged over one minute time periods and our correlation analysis is based on the compared temporal variabilities over short time periods, which cannot be affected by the removal of a constant noise.

[29] The most energetic particle fluxes were given by the MIMI LEMMS instrument, with the usage of C_0–C_7 channels for 18–832 keV electrons and of A_0–A_7 channels for 27–4000 keV ions (updated values since the original ones published by *Krimigis et al.* [2004]). All particles fluxes were averaged—to remove the variability induced by the noise—over 86 s (for SOI, when the LEMMS platform was rotating in 86 s) or 60s time bins (for the second period when the platform was static) and interpolated to the LP time steps used in section 3.2. The LEMMS data were corrected for the presence of light contamination, bad subsectors, and background (E. Roussos, private communication, 2012).

[30] Figure 3 shows the correlation between the temporal evolutions of the energetic current I_{ener} (derived in section 3.2) and the fluxes of electrons and ions as a function of energy. The Pearson's r correlation coefficient was derived from the linear regression between the energetic current and the particle fluxes considered.

[31] The correlation analysis during the SOI period alone with using the anode 5 CAPS ELS data revealed a peak near 400–600 eV. Considering the two periods together (SOI and high inclination orbit) determines the energy range of the

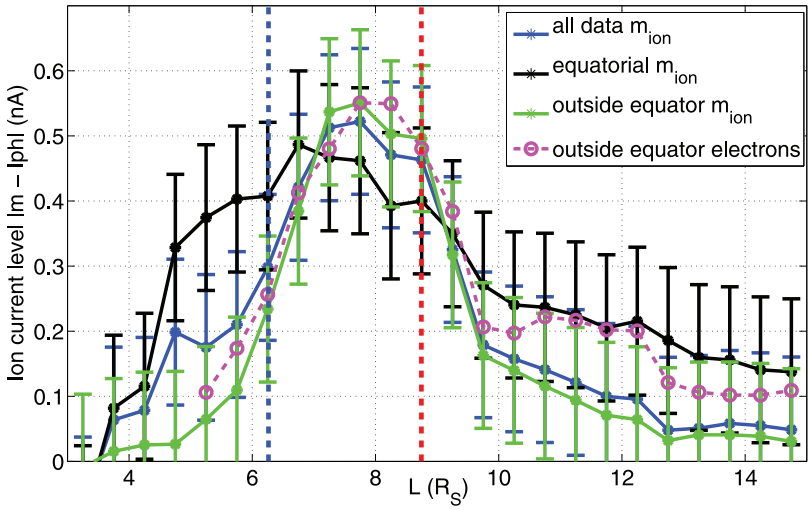

Figure 4. Radial profiles (L Shell values) of the ion current level—$m_{ion} = |m - I_{ph}|$ in nA—and of the normalized CAPS ELS electron differential number fluxes $(keV.\ cm^2.\ sr.\ s)^{-1}$ from anode 5, averaged over 10 minutes time bins and over the four energy channels from 253 up to 474 eV. These ELS data were normalized so that the maximum number flux is placed at the same ordinate value as the maximum value of m_{ion} in the figure. The thick blue and red vertical dashed lines show the L Shell values of Dione and Rhea. The data sets cover the period from February 1st 2005 to July 30rd 2008.

peak near 250–450 eV. By comparison, the correlations with low (IMS) or high energy (LEMMS) ions were small, indicating that the 250–450 eV magnetospheric electrons most probably generate the energetic current measured by the probe. It is important to consider long enough time periods, to avoid eventual secondary peaks related to the coincidental presence of several populations on the same field lines. In addition, another correlation analysis was also performed with fluxes averaged over all anodes for CAPS ELS (blue line with circles in Figure 3), but no significant change was observed. We may add that the scatterplots were analyzed, revealing no outliers for the 250–450 eV energies. A Fisher test [*Press et al.*, 2007] was also performed at all energies, which confirmed the statistical significance (for a significance level of 1%) of the linear regressions with respect to a null hypothesis—independence between the current and the particle fluxes—except for the worst correlations (e.g. for 3–7 eV or 60–90 eV electron energies).

[32] Moreover, the energy range of the source particles, compared with the secondary electron emission yield peak (with a yield above one) usually located near 200–1000 eV for metal layers [*Hastings and Garrett*, 1996; *Walters and Ma*, 2001; *Lorkiewicz et al.*, 2007], supports the conclusion that the energetic current I_{ener} is driven by the secondary electrons contribution. An example of such yield curve for a TiN surface [*Walters and Ma*, 2001] is plotted in yellow in Figure 3, revealing a similar peak energy near 300 eV. Our correlation analysis does however not provide the yield curve directly, which does not allow to compare both curves beyond the peak energy. Moreover, the exact composition and the treatment of the probe surface strongly affect the secondary electron emission yield curve (in particular the maximum yield value), which prevents us from using yield curves published previously to understand the exact behavior of the LP. We may also add that the impact by energetic ions is known to induce secondary electrons, but mostly at higher energies, above 10 keV [*Hastings and Garrett*, 1996] where the particle fluxes are much smaller than for 250–450 eV electrons.

4.2. The Spatial Distribution of the Secondary Electron Current Region

[33] The correlation analysis developed in the previous section demonstrated that energetic electrons (250–450 eV) in the magnetosphere are the most probable source of the enhanced current region observed in Figure 1, through the generation of a current I_{ener} dominated by the secondary electron component of I_{sec}*. However, why is there such a spatial distribution for the region observed, and can it give information about the magnetospheric dynamics ?

[34] Figure 4 shows the comparison between the ion current level $m_{ion} = |m - I_{ph}|$—previously mapped in Figure 1 and roughly equal to the energetic current off the equatorial plane—and the energetic electrons normalized (see figure caption) differential number fluxes off the equator ($|Z| > 1\ R_S$). We computed 3.5 years—same period as in section 2.2 from 2005 to 2008—of CAPS electron fluxes at energies near the peak for secondary electron emissions (i.e. from 253 to 474 eV, the lower and upper energy values of the respective bin numbers 30 and 27). The m_{ion} profiles off and near the equatorial plane are shown, along with the total profile. The error bars for the averaged profiles of m_{ion} are given by the combination of both the noise level of 0.11 nA (which affects every single measurement) and the standard deviation among all measurements of each L Shell bin.

[35] The m_{ion} radial profile displays a permanent peak between mostly $L = 6$ and $L = 10$, which is clearer off the equator, since current contributions other than I_{ener} may be significant near the equatorial plane (currents induced by dust or cold ions, see section 3). The full width at half maximum FWHM is given by the $L = 6.4$–9.4 range off the equator, but significant secondary electron currents may be observed

further out in the magnetosphere. The same curve is observed for both CAPS ELS fluxes and the current m_{ion}, thus confirming the energetic electrons as the source of the secondary electron current region. The combined absence of energetic electrons fluxes and of other significant particles (dust or cold plasma) off the equator induces small currents below the noise level beyond 11 R_S, whereas significant currents are measured by the LP near the equator even in the outer magnetosphere. An analysis of the Saturnian local time dependance for the energetic electron fluxes also shows the dayside/nightside asymmetry seen in Figure 1 for the current m_{ion}.

[36] This peak in the electrons near $L = 8$ is actually known since the Voyager data [*Sittler et al.*, 1983], and was confirmed recently by Cassini at low energies by *Young et al.* [2005] and *Schippers et al.* [2008] [see also *Rymer et al.*, 2007; *DeJong et al.*, 2010] and at higher energies corresponding to the outer electron radiation belt [*Carbary et al.*, 2009; *Kollmann et al.*, 2011]. *Rymer et al.* [2008] and *Schippers* [2009] interpreted the peak as due to an inward transport of electrons (possibly through interchange events) until these reach the inner magnetosphere where strong loss mechanisms occur (interactions with the neutral torus or the inner moons). The day-night asymmetry of the peak was also observed and attributed, at high energies, to nightside injections combined with a drift stagnation in a nondipolar Saturnian field [*Carbary et al.*, 2009], or, at lower energies, to stronger nightside interchange injections [*DeJong et al.*, 2011].

[37] Mapping the secondary electron current estimated from the LP may also bring some clues about the magnetospheric dynamics, through its sensitivity to energetic electrons. The secondary electron current region is indeed a complex key region, where the Saturnian outer auroral emission maps into the magnetosphere, an emission possibly induced by energetic electrons (in the energy range of hundreds eV to few keV [*Grodent et al.*, 2010]). Moreover, *Gurnett et al.* [2010] identified in this broad region a plasmapause-like boundary at high latitudes, with a strong density drop (up to three orders of magnitude) and most often a coincident separation between closed and open field lines.

[38] Figure 5 was adapted from *Gurnett et al.* [2010], who identified the location of this boundary on July 28*th* 2008, based on the electron density profile (derived from the floating potential of the LP, shown in Figure 5c; see *Morooka et al.* [2009] for more details on this derivation technique) and on the comparison between upward and downward electron fluxes from the MIMI LEMMS detectors (Figure 5d). Figure 5a shows the CAPS ELS fluxes from the same channels as in Figure 4, with two main peaks (near 9:30 and 14:30) corresponding to the crossings of the secondary electron current region and with large regions dominated by noise (penetrating radiations between 10:30 and 14:00, or the noise level with very few counts/s before 9:00 and after 14:40). Figure 5b shows both m and m_{ion} (given by $m_{ion} = |m - I_{ph}|$) currents measured by the LP: the m current is thus dominated by the photoelectron current (I_{ph}), except at the two main peaks where m_{ion} is large due to the dominant contribution from the energetic electrons. These two peaks correspond to the inbound/outbound crossings of the secondary electron current region mapped in the Figure 1. The absence of some data points for m_{ion} (e.g. before 9:00) corresponds to negative m_{ion} values, due to a slight overestimation of the photoelectron current estimate, for which there is always a possible systematic error (<0.1 nA) and a small random noise level (~0.05 nA; see section 2.1).

[39] This panel thus reveals that the boundaries identified by *Gurnett et al.* [2010] may also be visible in the m and m_{ion} currents, with a significant increase when entering the closed field lines region, at 9:00 and 14:40. The plasmapause-like boundary is revealed by strong density gradients [*Gurnett et al.*, 2010], which then drive a variability of the m current of the LP (the constant level is given by the photoelectron current): when the spacecraft is located inside the secondary electron current region and off the equator, i.e. near the two main peaks at 9:30 and 14:30, the energetic population is the main magnetospheric population—the cold plasma is centrifugally confined near the equator—and its dynamics drives the variabilities of both the density and the m or *mion* currents (because of the secondary electrons current produced).

[40] This case study suggests that we may locate the plasmapause-like boundary identified by *Gurnett et al.* [2010] through the analysis of the m current of the LP. More precisely, this determination of the boundary may be done as long as the associated density gradient can be seen in the measured current, i.e. as long as the boundary is located in a region with dense plasma or strong energetic electron fluxes (such as the secondary electron current region). As a consequence, the boundary should be located at the outer edge of the secondary electron current region or beyond. This plasmapause-like boundary may also be the separation between closed and open field lines (this was the case on July 28th 2008), as most often observed by *Gurnett et al.* [2010]. However, if Dungey-like convection similar to Earth exists at Saturn, both boundaries will not be coincident.

5. Conclusions and Perspectives

[41] This study addresses the effects of the impact of energetic particles (electrons) on the Langmuir Probe (LP) current-voltage curve and describes a method to identify the secondary current contribution due to impacting particles.It reveals the capability for the Cassini LP to detect energetic electrons, beyond its classical usage in cold and dense plasma regions.

[42] The current measured for negative potentials (positive ions being attracted) in Saturn's magnetosphere during several years (2005–2008) showed indeed the presence of a permanent broad region of enhanced current whose maximum is in the L Shell range of ~6–10, with a FWHM in the range of L = 6.4–9.4 and significant values which can be measured further out in the magnetosphere. This region displays a day-night asymmetry and is created by the impact of 250–450 eV magnetospheric electrons inducing a current of secondary electrons leaving the probe. The mapping of the energetic electrons fluxes at these energies as measured by CAPS/ELS revealed the same spatial distribution (both the radial profile and the local time asymmetries). This feature is actually already known for electrons since the Voyager data [*Sittler et al.*, 1983] and is possibly induced by the inward transport and heating of particles through interchange events as far as the loss regions of the inner magnetosphere [*Schippers et al.*, 2008; *DeJong et al.*, 2011].

[43] A case study suggests that the analysis of the LP current for negative potentials can help to locate the plasmapause-like

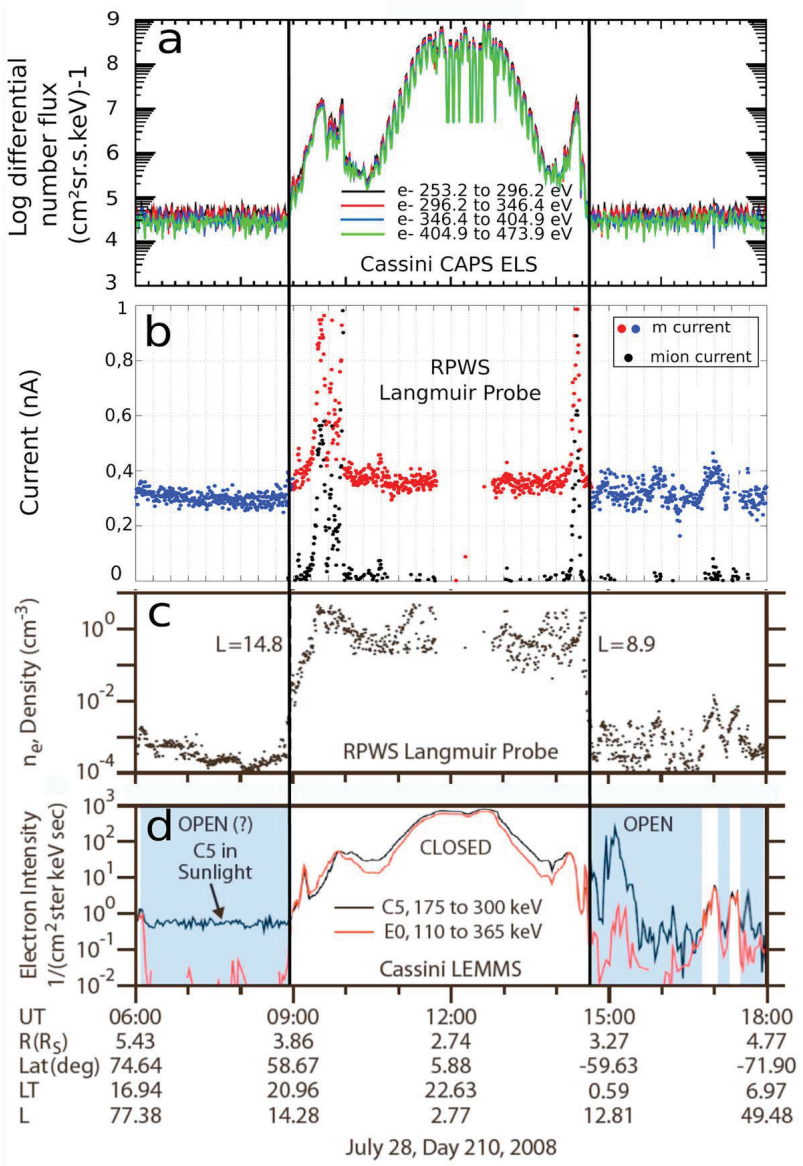

Figure 5. Multi-instruments plot showing closed and open-field lines regions on July 28th 2008. (a) CAPS ELS electron differential number fluxes from anode 5 of the four energy channels from 253 up to 474 eV. (b) *m* (blue/red: open/closed field lines region) and m_{ion} (black) currents from the LP. The lower two panels were published in *Gurnett et al.* [2010]: (c) the electron density given by the LP and (d) the intensities in channels *C*5 and *E*0 of two MIMI LEMMS telescopes oriented such that they measured ~200 keV electrons moving in opposite directions along the magnetic field. The time (*UT*), distance from Saturn (*R*), latitude (*LAT*), local time (*LT*) and *L* Shell parameter are shown.

boundary identified by *Gurnett et al.* [2010] at high latitudes, and that it should be located at the outer edge of the secondary electron current region or beyond. This boundary may be coincident with the separation between closed and open magnetic field lines, unless Dungey-like convection similar to Earth exists at Saturn.

[44] Future work will provide details on the estimation of the exact yield curve as a function of the energy of impacting particles for the Cassini LP (only the peak energy was obtained here). We will also investigate how to correct the LP data analysis for the current by energetic electrons which is essentially a noise for cold plasma studies: deriving the cold plasma currents in the peak region needs a precise knowledge of the current induced by energetic electrons. Such knowledge would be very useful for future missions with similar Langmuir probes (e.g. JUICE at Jupiter, Bepi-Colombo at Mercury, Rosetta at the comet Churyumov-Gerasimenko).

[45] **Acknowledgments.** We would like to thank Rob Wilson and Elias Roussos for their help with the CAPS and LEMMS data, respectively. The RPWS/LP efforts are supported by the Swedish National Space Board (SNSB).

[46] Masaki Fujimoto thanks Jean-Pierre Lebreton and another reviewer for their assistance in evaluating this paper.

References

Ågren, K., et al. (2007), On magnetospheric electron impact ionisation and dynamics in Titan's ram-side and polar ionosphere–a Cassini case study, *Ann. Geophys.*, *25*, 2359–2369.

Ågren, K., et al. (2011), Detection of currents and associated electric fields in Titan's ionosphere from Cassini data, *J. Geophys. Res.*, *116*, A04313, doi:10.1029/2010JA016100.

Arridge, C. S., et al. (2009), The effect of spacecraft radiation sources on electron moments from the Cassini CAPS electron spectrometer, *Planet. Space Sci.*, *57*, 854–869, doi:10.1016/j.pss.2009.02.011.

Carbary, J., D. Mitchell, N. Krupp, and S. Krimigis (2009), L shell distribution of energetic electrons at Saturn, *J. Geophys. Res.*, *114*, A09210, doi:10.1029/2009JA014341.

DeJong, A., J. Burch, J. Goldstein, A. Coates, and D. T. Young (2010), Low-energy electrons in Saturn's inner magnetosphere and their role in interchange injections, *J. Geophys. Res.*, *115*, A10229, doi:10.1029/2010JA015510.

DeJong, A., J. Burch, J. Goldstein, A. Coates, and F. Crary (2011), Day-night asymmetries of low-energy electrons in Saturn's inner magnetosphere, *Geophys. Res. Lett.*, *38*, L08106, doi:10.1029/2011GL047308.

Dudok de Wit, T., M. Kretzschmar, J. Lilensten, and T. Woods (2009), Finding the best proxies for the solar UV irradiance, *Geophys. Res. Lett.*, *36*, L10107, doi:10.1029/2009GL037825.

Edberg, N., J.-E. Wahlund, K. Ågren, M. Morooka, R. Modolo, C. Bertucci, and M. Dougherty (2010), Electron density and temperature measurements in the cold plasma environment of Titan: Implications for atmospheric escape, *Geophys. Res. Lett.*, *37*, L20105, doi:10.1029/2010GL044544.

Edberg, N., et al. (2011), Structured ionospheric outflow during the Cassini T55–T59 Titan flybys, *Planet. Space Sci.*, *59*, 788–797, doi:10.1016/j.pss.2011.03.007.

Fahleson, U., C.-G. Fälthammar, and A. Pedersen (1974), Ionospheric temperature and density measurements by means of spherical double probes, *Planet. Space Sci.*, *22*, 41–66.

Garnier, P., et al. (2009), Titan's ionosphere in the magnetosheath: Cassini RPWS results during the T32 flyby, *Ann. Geophys.*, *27*, 4257–4272.

Grodent, D., A. Radioti, B. Bonfond, and J.-C. Gerard (2010), On the origin of Saturn's outer auroral emission, *J. Geophys. Res.*, *115*, A08219, doi:10.1029/2009JA014901.

Gurnett, D., et al. (2004), The Cassini radio and plasma wave investigation, *Space Sci. Rev.*, *114*, 395–463, doi:10.1007/s11214-004-1434-0.

Gurnett, D., et al. (2010), A plasmapause-like density boundary at high latitudes in Saturn's magnetosphere, *Geophys. Res. Lett.*, *37*, L16806, doi:10.1029/2010GL044466.

Gustafsson, G., and J.-E. Wahlund (2010), Electron temperatures in Saturn's plasma disc, *Planet. Space Sci.*, *58*, 1018–1025, doi:10.1016/j.pss.2010.03.007.

Hastings, D., and H. Garrett (1996), *Spacecraft-Environment Interactions*, 292 pp., Cambridge Univ. Press, Cambridge, U. K.

Holmberg, M. (2010), Determination of solar EUV intensity and ion flux from Langmuir probe current characteristics, MS thesis, Uppsala Univ., Uppsala, Sweden. [Available at http://www.essays.se/essay/ff01166d6b/.]

Jacobsen, K., J.-E. Wahlund, and A. Pedersen (2009), Cassini Langmuir probe measurements in the inner magnetosphere of Saturn, *Planet. Space Sci.*, *57*, 48–52, doi:10.1016/j.pss.2008.10.012.

Kollmann, P., E. Roussos, C. Paranicas, N. Krupp, C. M. Jackman, E. Kirsch, and K. Glassmeier (2011), Energetic particle phase space densities at Saturn: Cassini observations and interpretations, *J. Geophys. Res.*, *116*, A05222, doi:10.1029/2010JA016221.

Krimigis, S. M., et al. (2004), Magnetosphere Imaging Instrument (MIMI) on the Cassini mission to Saturn/Titan, *Space Sci. Rev.*, *114*, 233–329, doi:10.1007/s11214-004-1410-8.

Lorkiewicz, J., J. Kula, S. Pszona, J. Sobczak, and A. Bilinski (2007), Sublimation TiN coating of RF power components, in *Proceedings of AIP International Conference on Research and Applications of Plasmas*, vol. 993, 411–414, Am. Inst. of Phys., Melville, N. Y., doi:10.1063/1.2909163.

McIlwain, C. (1961), Coordinates for mapping the distribution of magnetically trapped particles, *J. Geophys. Res.*, *66*, 3681–3691.

Modolo, R., J.-E. Wahlund, R. Bostrom, P. Canu, W. S. Kurth, D. Gurnett, G. Lewis, and A. Coates (2007), The far plasma wake of Titan from the RPWS observations: A case study, *Geophys. Res. Lett.*, *34*, L24S04, doi:10.1029/2007GL030482.

Morooka, M. W., et al. (2009), The electron density of Saturn's magnetosphere, *Ann. Geophys.*, *27*, 2971–2991, doi:10.5194/angeo-27-2971-2009.

Morooka, M. W., J.-E. Wahlund, A. I. Eriksson, W. M. Farrell, D. A. Gurnett, W. S. Kurth, A. M. Persoon, M. Shafiq, M. André, and M. K. G. Holmberg (2011), Dusty plasma in the vicinity of Enceladus, *J. Geophys. Res.*, *116*, A12221, doi:10.1029/2011JA017038.

Mott-Smith, H. M., and I. Langmuir (1926), The theory of collectors in gaseous discharges, *Phys. Rev*, *28*, 727–763, doi:10.1103/PhysRev.28.727.

Persoon, A., et al. (2009), A diffusive equilibrium model for the plasma density in Saturn's magnetosphere, *J. Geophys. Res.*, *114*, A04211, doi:10.1029/2008JA013912.

Press, W. H., et al. (2007), *Numerical Recipes: The Art of Scientific Computing*, 3rd ed., Cambridge Univ. Press, Cambridge, U. K.

Rosenqvist, L., J.-E. Wahlund, K. Ågren, R. Modolo, H. Opgenoorth, D. Strobel, I. Müller-Wodarg, P. Garnier, and C. Bertucci (2009), Titan ionospheric conductivities from Cassini measurements, *Planet. Space Sci.*, *57*, 1828–1833, doi:10.1016/j.pss.2009.01.007.

Rymer, A., et al. (2007), Electron sources in Saturn's magnetosphere, *J. Geophys. Res.*, *112*, A02201, doi:10.1029/2006JA012017.

Rymer, A., B. Mauk, T. Hill, C. Paranicas, D. Mitchell, A. Coates, and D. Young (2008), Electron circulation in Saturn's magnetosphere, *J. Geophys. Res.*, *113*, A01201, doi:10.1029/2007JA012589.

Schippers, P. (2009), Etude de l'équilibre et de la circulation des populations d'électrons dans la magnétosphère de Saturne à l'aide des données multi-instrumentales de la sonde Cassini-Huygens, PhD thesis, Univ. Paul Sabatier, Toulouse, France.

Schippers, P., et al. (2008), Multi-instrument analysis of electron populations in Saturn's magnetosphere, *J. Geophys. Res.*, *113*, A07208, doi:10.1029/2008JA013098.

Sittler, E., K. Ogilvie, and J. Scudder (1983), Survey of low energy plasma electrons in Saturn's magnetosphere: Voyagers 1 and 2, *J. Geophys. Res.*, *88*, 8848–8870.

Sittler, E., et al. (2006), Cassini observations of Saturn's inner plasmasphere: Saturn orbit insertion results, *Planet. Space Sci.*, *54*, 1197–1210, doi:10.1016/j.pss.2006.05.038.

Sittler, E., et al. (2008), Ion and neutral sources and sinks within Saturn's inner magnetosphere: Cassini results, *Planet. Space Sci.*, *56*, 3–18, doi:10.1016/j.pss.2007.06.006.

Tapping, K. (1987), Recent solar radio astronomy at centimeter wavelengths: The temporal variability of the 10.7-cm flux, *J. Geophys. Res.*, *93*, 829–838.

Thomsen, M., D. Reisenfeld, D. Delapp, R. Tokar, D. Young, F. Crary, E. Sittler, M. McGraw, and J. Williams (2010), Survey of ion plasma parameters in Saturn's magnetosphere, *J. Geophys. Res.*, *115*, A10220, doi:10.1029/2010JA015267.

Wahlund, J., et al. (2005a), Cassini measurements of cold plasma in the ionosphere of Titan, *Science*, *308*, 986–989, doi:10.1126/science.1109807.

Wahlund, J.-E., et al. (2005b), The inner magnetosphere of Saturn: Cassini RPWS cold plasma results from the first encounter, *Geophys. Res. Lett.*, *32*, L20S09, doi:10.1029/2005GL022699.

Wahlund, J.-E., et al. (2009), Detection of dusty plasma near the E-ring of Saturn, *Planet. Space Sci.*, *57*, 1795–1806, doi:10.1016/j.pss.2009.03.011.

Walters, D., and Q. Ma (2001), Secondary electron yield of a thin film coating on the APS RF cavity tuners, in *Proceedings of the 2001 Particle Accelerator Conference*, vol. 3, pp. 2153–2155, IEEE Press, Piscataway, N. J.

Young, D., et al. (2004), Cassini plasma spectrometer investigation, *Space Sci. Rev.*, *114*, 1–112, doi:10.1007/s11214-004-1406-4.

Young, D. T., et al. (2005), Composition and dynamics of plasma in Saturn's magnetosphere, *Science*, *307*, 1262–1266, doi:10.1126/science.1106151.